Journal of Energy Storage 77 (2024) 109975

Contents lists available at ScienceDirect

Journal of Energy Storage

journal homepage: www.elsevier.com/locate/est

Research papers

Design and optimization of metal hydride reactor with phase change material using fin factor for hydrogen storage

Ankush Parmanand Shrivastav [a], Praveen Kumar Kanti [a,*], G. Mohan [b], M.P. Maiya [a,*]

[a] Department of Mechanical Engineering, Indian Institute of Technology Madras, Chennai 600036, India
[b] Centre for Computational Research in Clean Energy Technologies, Sree Chitra Thirunal College of Engineering, Kerala, Thiruvananthapuram 695018, India

ARTICLE INFO

Keywords:
Absorption
Buoyancy
Fin efficiency
Hydrogen storage
Magnesium
Performance evaluation criterion

ABSTRACT

The solid-state hydrogen storage in metal hydride (MH) is safer and energy efficient than the gaseous and liquid storage methods. The absorption of hydrogen in MH is highly exothermic. Hence, a good heat management system is required to increase the charging rate. The phase change material (PCM) can be integrated into the reactor to reuse the absorption heat for hydrogen desorption. The present numerical study models the concentric cylindrical reactor with magnesium (Mg) as MH surrounded by sodium nitrate ($NaNO_3$) as PCM using COMSOL Multiphysics v6.1. The effect of buoyancy inside the PCM domain is investigated. An iterative approach is used to determine the required amount of PCM. Copper fins are added inside both MH and PCM. The effect of the number of fins, corresponding fin thickness and pitch on hydrogen absorption are determined to optimize the MH reactor. The outcomes reveal that the hydrogen absorption rate increases with fin numbers. The reactor with 10 and 30 fins takes 86.5 and 97.3 % less time than without fins for 90 % hydrogen absorption, respectively. The novel approach is proposed to estimate the fin efficiency (η_f) using temperature profiles of MH and fin during prevailing unsteady heat and mass transfer. The fin factor (F_f) is presented using the η_f and mass of MH. The performance evaluation criterion (PEC) is discussed based on hydrogen absorption relative to the system's weight. Further, the effect of operating parameters like hydrogen supply pressure and the initial temperature is studied on the reactor performance.

1. Introduction

A significant portion of the world's current energy consumption is derived from various fossil fuels, which are finite in their availability. Their utilization not only contributes to environmental pollution but also results in the emission of greenhouse gases, which in turn leads to global warming. Fossil fuels supply nearly 80 % of the world's primary energy [1]. This has an adverse effect on the global climate. Furthermore, the continuous growth of the global population leads to an escalating demand for energy. As a response to these critical challenges, researchers are increasingly prioritizing the exploration and development of renewable and sustainable energy sources to address the world's growing energy demands while mitigating the environmental impact. Hydrogen is a possible candidate to support these sources as an energy carrier due to its inherent cleanliness, remarkable efficiency, and abundant presence in compound form. Extensive research efforts have been dedicated to harnessing hydrogen's potential, particularly in applications such as fuel cells [2] and internal combustion engines [3].

Hydrogen is a clean-burning fuel. Due to its very high energy density, which is more than four times of anthracite coal [4], hydrogen is of great interest to researchers. However, its efficient storage method is critical in the energy chain. The advantage of safety and high volumetric storage capacity of solid-state hydrogen storage is highly beneficial compared to gas and liquid storage methods. Several works have been reported on low-temperature-based MH, like lanthanum (La) [5] and mischmetal (Mm) [6]. Due to their high hydrogen storage capacity, magnesium (Mg) [7] based high-temperature MHs are of great interest. The storage capacity of MgH_2 can be up to 7.6 wt% [8]. The enthalpy of formation of MgH_2 is 75 kJ/mol of H_2, which needed to be removed or added during absorption or desorption, respectively.

Hydrogen storage is a heat-driven and mass-transfer process requiring a proper heat management method. To achieve this, researchers incorporated heat transfer fluid (HTF) [9,10], fins with HTF [11], circular fins [12], perforated radial fins with HTF [13], metal foams (MFs) like aluminum foam [14,15], copper foam [16], etc. Many works [17,18] used PCM as energy storage media for proper energy utilization.

* Corresponding authors.
E-mail address: mpmaiya@iitm.ac.in (M.P. Maiya).

https://doi.org/10.1016/j.est.2023.109975
Received 7 July 2023; Received in revised form 6 November 2023; Accepted 2 December 2023
Available online 12 December 2023

Nomenclature

A	van't Hoff constant
B	van't Hoff constant, K
C	reaction rate constant, s^{-1}
C_p	specific heat capacity, J kg^{-1} K^{-1}
E	activation energy, J mol^{-1}
F	force, N
F_f	fin factor
f	liquid fraction
g	acceleration due to gravity, m s^{-2}
h	height, m
k	thermal conductivity, W m^{-1} K^{-1}
L	latent heat of PCM, J kg^{-1}
M	molecular mass of hydrogen, kg mol^{-1}
m	mass, kg
n	unit area vector
P	pressure, Pa
p	pitch, m
$\dot{Q}$	heat transfer rate, W
q	heat flux, W m^{-2}, also mass and concentration flux in Eq. (26)
R	universal gas constant, J mol^{-1} K^{-1}
r	radial coordinate, m
$\dot{S}$	source, W m^{-3}
T	temperature, K
t	time, s
t_f	fin thickness, m
u	velocity vector, m s^{-1}
V	volume, m^3
wt	maximum hydrogen storage capacity, %
x	reaction fraction
z	longitudinal coordinate, m

Greek letters

α	phase transition function
β	thermal expansion coefficient, K^{-1}
ϵ	porosity
ΔH	reaction enthalpy, J mol^{-1}
η	efficiency
μ	dynamic viscosity, mPa·s
ρ	density, kg m^{-3}

Subscripts

0	initial condition
abs	absorption
des	desorption
eff	effective
eq	equilibrium
f	fin
g	gas
l	liquid
ref	reference
s	solid

Abbreviations

HTF	heat transfer fluid
MF	metal foam
MH	metal hydride
PCM	phase change material
PEC	performance evaluation criterion
LMTD	log mean temperature difference

One of the most practical ways to retain the heat released during hydrogen absorption [12,19] and reuse it during desorption [20] is by employing PCM as an energy storage medium. During its phase change, it stores energy. MH reactors using PCMs have been the subject of several recent investigations [21,22]. These studies examined how the PCM's thermophysical characteristics affect MH behavior. For the efficient MH-PCM system, the chosen PCM should have a melting temperature in the operating range, higher enthalpy and more excellent thermal conductivity.

Aadhithiyan et al. [23] optimized the performance of the MH reactor ($LaNi_5$) having helical coils using single and multi-objective optimization based on weight ratio and thermal performance. Krisha et al. [24] performed numerical study to optimize the number of longitudinal fins in $LaNi_5$ filled MH reactor and concluded that adding 8 fins is optimal for better heat transfer. Afzal et al. [25] conducted transient simulation studies on shell and tube reactors having $LaNi_5$ to study the ab/desorption characteristics. They proposed a parameter based on heat transfer capacity against system weight, which optimizes the number of MH tubes required. Bai et al. [26] compared the hydrogen absorption performance of the $LaNi_5$ reactor by adding uniform and gradient porosity MF. They concluded that the optimized two-layers of gradient porosity MF reactor's performance increased by 11.5 % relative to the uniform MF reactor. Arumuru et al. [27] performed an experimental study to evaluate the effectiveness of heat sinks using synthetic jets and PCM by varying the design parameters like PCM ball diameters and water flow rate. They found that the heat sink with PCM performed better as compared to those without PCM by maintaining a lower base temperature due to the latent heat storage of PCM.

Darzi et al. [28] investigated the behavior of a $LaNi_5$ MH reactor integrated with the Rubitherm PCM. A metal foam was incorporated into the PCM jacket. They reported that the ab/desorption times decreased, respectively by considering a high inlet and low outlet pressure and by adding metal foam in the PCM jacket. Chibani et al. [29] determined the desorption performance of the $LaNi_5$ reactor with MFs (Al, Cu, Ni, and Ti) and PCM by performing a numerical study. The presence of MF-PCM improves the MH performance by releasing its latent heat to the MH bed, and it is completely discharged within 700 s. Finally, they reported that higher conductivity with low porous MFs improves PCM solidification and the tube position plays a significant role. Nguyen et al. [30] conducted experiments to analyze the hydrogen charging and discharging of the mischmetal alloy MmNiMnCo MH reactor with and without RT28HC paraffin as PCM. In the case of PCM, MH's hydrogen absorption and desorption are two times greater than without PCM. They also reported that the addition of copper foam to PCM improves the effective thermal conductivity and leads to the enhancement of MH's charging and discharging performances.

Most of the research considered the cylindrical reactor having MH surrounded by PCM and agreed that such hydrogen storage systems are energy efficient. However, most of them neglected both the buoyancy effect in PCM and sensible heat for calculating its mass. The present study investigates the hydrogen absorption and the effective heat transfer performance of the MH (Mg) - PCM ($NaNO_3$) hydrogen storage system. A mathematical model describing kinetics, momentum and heat transfer in MH and PCM is first developed. The effect of buoyancy on performance parameters (hydrogen absorption, liquid fraction of PCM and temperature) and a methodology to calculate the required amount of PCM to store the energy are presented. The fins are added to increase the effective heat transfer from MH to PCM. The log mean temperature difference (LMTD) approach is used to determine the fin efficiency. A new parameter known as the fin factor is used to optimize the number of fins. PEC is presented as the new criterion based on the hydrogen absorption and weight of the system. Finally, the impact of hydrogen

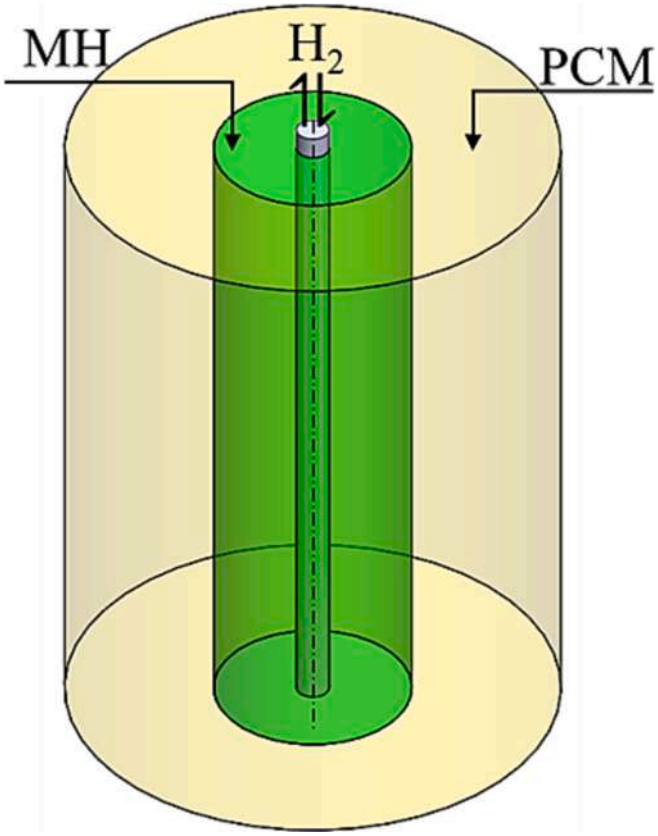

Fig. 1. 3D model of MH surrounded by PCM.

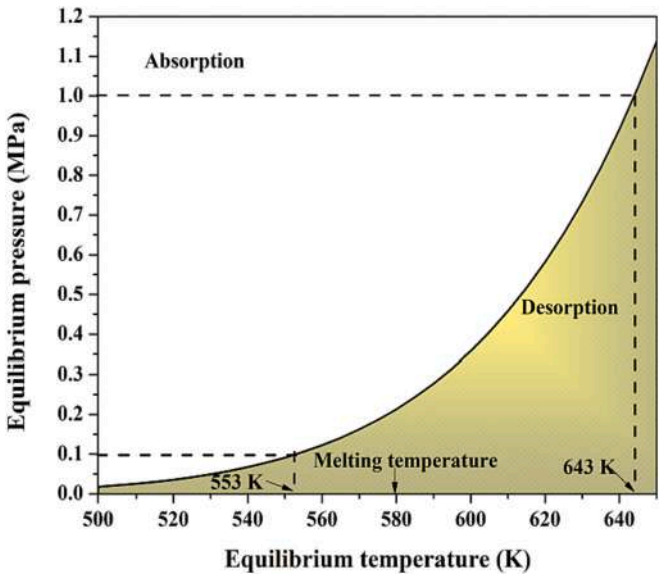

Fig. 2. Equilibrium pressure-temperature plot of MgH_2 [31].

supply pressure and the initial temperature is studied.

2. Model description

Fig. 1 shows the 3D model of MH-surrounded PCM. The design consists of concentric inner and outer cylinders filled with MH and PCM, respectively. The absorption and desorption of hydrogen follow exothermic and endothermic reactions, respectively, presented by Eq. (1):

Table 1
Thermophysical properties of MH and PCM.

Sl. No.	Properties	MH [32,33]	PCM [34]	
			Solid	Liquid
1	Density, ρ [kg m^{-3}]	1800	2113	1908
2	Specific heat capacity, C_p [J kg^{-1} K^{-1}]	1545	1655	1655
3	Thermal conductivity, k [W m^{-1} K^{-1}]	0.48	0.6	0.514
4	Absorption rate constant, C_a [s^{-1}]	10^{10}	–	
5	Activation energy, E_a [kJ mol^{-1}]	130	–	
6	Maximum hydrogen storage capacity, wt [%]	6	–	
7	Porosity, ϵ	0.5	–	
8	Reaction enthalpy, ΔH [J mol^{-1}]	75,000	–	
9	Reaction entropy, ΔS [J mol^{-1} K^{-1}]	135.6	–	
10	Dynamic viscosity, μ [mPa·s]	–	–	3
11	Latent heat, L [kJ kg^{-1}]	–	178	

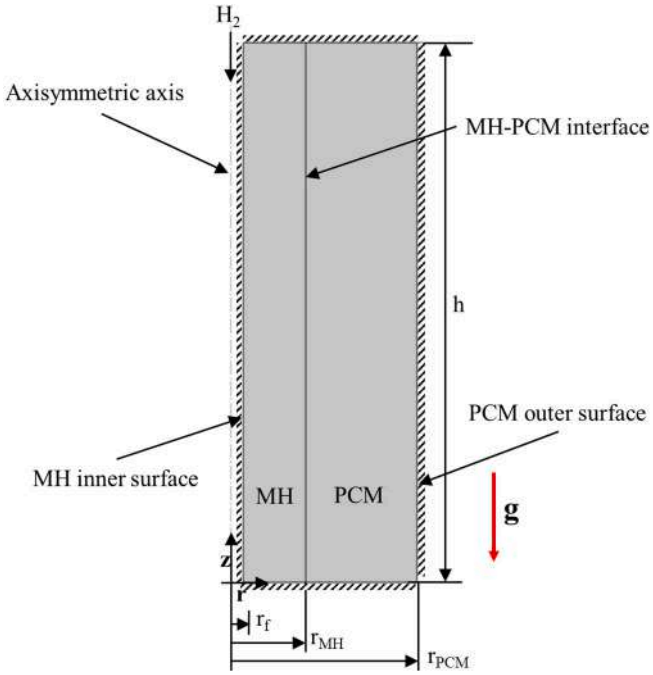

Fig. 3. 2D axisymmetric model of MH encircled by PCM.

$$M + \frac{x}{2}H_2 \leftrightarrow MH_x + \Delta H \quad (1)$$

This investigation considers 500 g of MH, which can store 30 g of hydrogen. The absorption and desorption pressures are set to 1 and 0.1 MPa [31], respectively. The corresponding equilibrium temperatures are 370 and 280 °C, respectively, as illustrated in Fig. 2. Since the melting temperature of $NaNO_3$ is 306 °C, which falls in the range of two equilibrium temperatures, it can facilitate both absorption and desorption. Table 1 lists the properties of MH and PCM used in this analysis.

3. Mathematical model

Fig. 3 refers to the 2D axisymmetric model of the computational domain considered. The following assumptions are made:

- Hydrogen is an ideal gas.
- The hydrogen pressure is uniform in the bed.
- The thermophysical properties of MH are constant and isotropic.
- The gas and the solid MH are locally in thermal equilibrium.
- The thermal resistance of the metallic wall is negligible.
- The volumetric change of the MH bed during absorption is neglected.

Table 2
Geometry parameters.

Sl. No.	Parameters	Value [mm]
1	Filter radius, r_f	5
2	MH tube radius, r_{MH}	29.5
3	PCM outer shell radius, r_{PCM}	75
4	Height of reactor, h	208.8

The dimensions of the reactor are provided in Table 2.

3.1. Governing equations

3.1.1. MH reactor

The energy equation used to evaluate the temperature of the reactor is as follows:

$$(\rho C_p)_{eff}\frac{\partial T}{\partial t} = \nabla\cdot(\nabla k_{eff} T) + \dot{S} \tag{2}$$

where $(\rho C_p)_{eff}$ is the effective heat capacity per unit volume, k_{eff} is the effective thermal conductivity and $\dot{S}$ is the source term. They are defined as follows:

$$(\rho C_p)_{eff} = \epsilon(\rho C_p)_g + (1-\epsilon)(\rho C_p)_{MH} \tag{3}$$

$$k_{eff} = \epsilon k_g + (1-\epsilon)k_{MH} \tag{4}$$

$$\dot{S} = \rho_{MH}\cdot wt\cdot(1-\epsilon)\cdot\frac{\Delta H}{M}\cdot\frac{\partial x}{\partial t} \tag{5}$$

The reaction equilibrium pressure P_{eq} at any temperature is related via van't Hoff equation as follows [35]:

$$ln\left(\frac{P_{eq}}{P_{ref}}\right) = A - \left(\frac{B}{T}\right) \tag{6}$$

where P_{ref} is 0.1 MPa and A and B are the reaction constants that depend on the entropy and enthalpy of the reaction, respectively, and they are defined as:

$$A = \frac{\Delta S}{R} \text{ and } B = \frac{\Delta H}{R} \tag{7}$$

The kinetic reaction for Mg for absorption and desorption is described using the following equations [36]:

$$\frac{\partial x}{\partial t} = C_{abs}exp\left(-\frac{E_{abs}}{RT}\right)\cdot\frac{P_g - P_{eq}}{P_{eq}}\cdot\frac{x-1}{2ln(1-x)}; P_g > 2P_{eq} \tag{8}$$

$$\frac{\partial x}{\partial t} = C_{abs}exp\left(-\frac{E_{abs}}{RT}\right)\cdot\frac{P_g - P_{eq}}{P_{eq}}\cdot(1-x); P_{eq} < P_g < 2P_{eq} \tag{9}$$

3.1.2. PCM

The apparent heat capacity method is used to model the PCM, which solves solid and liquid phases using effective material properties with a single heat transfer equation. The heat capacity is modified by using the latent heat of phase change. The properties of the PCM in the mushy zone are characterized using the Heaviside function.

The conservation of mass can be described by continuity equation as [37]:

$$\frac{\partial \rho}{\partial t} + \nabla\cdot(\rho \boldsymbol{u}) = 0 \tag{10}$$

The Navier-Stokes equation in buoyancy-driven flow with the Boussinesq approximation [38] can be defined as follows:

$$\rho\frac{\partial \boldsymbol{u}}{\partial t} + \rho(\boldsymbol{u}\cdot\nabla)\boldsymbol{u} = \mu\nabla^2\boldsymbol{u} - \nabla P + S + F_b \tag{11}$$

where S is the momentum source term and F_b is the body force term given by Eqs. (12) and (13), respectively [39]:

$$S = A_m \boldsymbol{u}\frac{(1-f)^3}{f^3+\gamma} \tag{12}$$

where f is the liquid fraction, $\gamma = 0.001$ (to make the Eq. (12) consistent when f is zero) and A_m is the mushy zone constant, it influences the morphology of the mushy region, and its value is considered in the present study as $5{\cdot}10^6$ [kg m^{-3} s^{-1}] [40].

$$F_b = \rho g\left(1-\beta(T-T_{ref})\right) \tag{13}$$

where T_{ref} is the reference temperature and is equal to the melting temperature T_m [37] and β is the thermal expansion coefficient defined by Eq. (14).

$$\beta = -\frac{1}{\rho}\frac{\partial \rho}{\partial T} \tag{14}$$

The energy equation in the PCM is as follows [41]:

$$\frac{(\rho C_p)_{eff}\partial T}{\partial t} + (\rho C_p)_{eff,PCM}\boldsymbol{u}\cdot\nabla T = \nabla\cdot(\nabla k_{eff,PCM} T) \tag{15}$$

where $(\rho C_p)_{eff,\ PCM}$ and $k_{eff,\ PCM}$ are the effective volumetric apparent heat capacity and thermal conductivity of PCM presented by Eqs. (16) and (17), respectively.

$$(\rho C_p)_{eff,PCM} = \frac{(1-f)(\rho C_p)_s + f(\rho C_p)_l}{\rho_{eff,PCM}} + L\frac{\partial \alpha}{\partial t} \tag{16}$$

$$k_{eff,PCM} = (1-f)k_s + fk_l \tag{17}$$

where $\rho_{eff,PCM}$ and α are the effective density of the PCM and the phase transition function capable of smooth transition between the solid and liquid phases defined by Eqs. (18) and (19), respectively [41].

$$\rho_{eff,PCM} = (1-f)\rho_s + f\rho_l \tag{18}$$

$$\alpha = \frac{1}{2}\cdot\frac{f\rho_l - (1-f)\rho_s}{\rho_{eff,PCM}} \tag{19}$$

The liquid fraction f denotes the amount of PCM melted as the function of temperature. The liquid fraction in the present study is defined using the Heaviside function inside the mushy zone.

$$f(T) = \begin{cases} 0, if\ T < T_m - \dfrac{\Delta T_{s\to l}}{2} \\ 1, if\ T > T_m + \dfrac{\Delta T_{s\to l}}{2} \end{cases} \tag{20}$$

where T_m is the melting temperature equivalent to 306 °C [34] and $\Delta T_{s\to l}$ denotes the transition temperature from solid to liquid phase equivalent to 1 °C [34].

3.2. Initial conditions

The initial temperature of the whole reactor is assumed to be constant, and the density of MH and the pressure are uniform:

$$T_0 = 300°C, P_0 = 1 \text{ MPa and } \rho_{MH} = \rho_0 \tag{21}$$

3.3. Boundary conditions

The constant heat flux boundary conditions between MH-PCM surface [42]:

$$k_{MH}\ \nabla T_{MH}\cdot\mathbf{n} = k_{eff}\ \nabla T_{PCM}\cdot\mathbf{n} \tag{22}$$

The interface boundary condition ensures that heat transfer between layers with different materials occurs smoothly by maintaining

Table 3
Number of elements in various grids.

Grid	Domain elements	Boundary elements
Grid 1	6720	516
Grid 2	14,839	769
Grid 3	26,226	1025
Grid 4	58,938	15,636

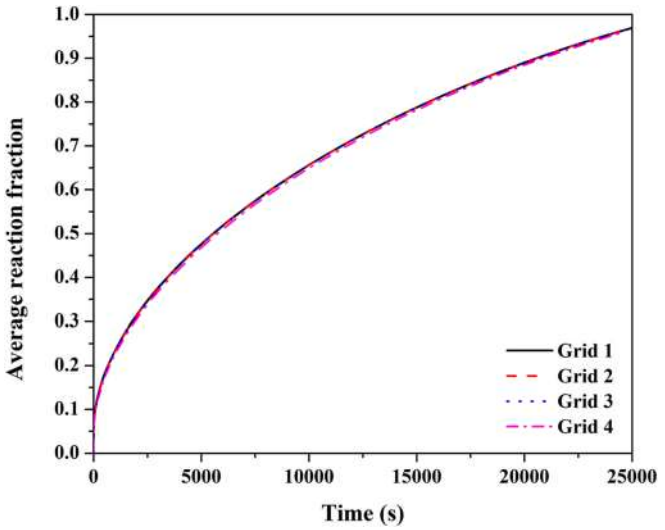

Fig. 4. Grid independence test.

temperature continuity at the interfaces. The temperature at the point of contact between two bodies in direct contact should be identical. This condition is defined as follows:

$$T_{MH}(r_{MH}, z, t) = T_{PCM}(r_{MH}, z, t) \tag{23}$$

The PCM's outer surface and MH's inner surface are considered insulated [42]:

$$\nabla T \cdot \boldsymbol{n} = 0 \tag{24}$$

The no-slip boundary conditions are imposed on the walls that surround the PCM.

4. Simulation methodology

The domains for MH and PCM are created as the 2D axisymmetric model in COMSOL Multiphysics v6.1. The fully coupled solver solves the conservation equations of mass, momentum and energy. A small tolerance value gives more accurate results with negligible error. Thus, the relative tolerance for all the variables is set to 10^{-6} as the convergence criterion.

The present study uses structured mesh elements to reduce computational time. To resolve the physics along the no-slip boundaries for the convection effect in the PCM domain, the boundary layer mesh is used at the walls. The boundary layer mesh consists of 8 layers and a stretching factor of 1.2. Four grids are used, and the number of elements in them is tabulated in Table 3. Fig. 4 displays the grid independence test for different mesh elements. The average reacted fraction is almost the same for the model with different grids. Therefore, in order to save computational time, Grid 1 is taken as the optimum mesh.

5. Results and discussion

5.1. Model validation

The mathematical model is solved using COMSOL Multiphysics v6.1,

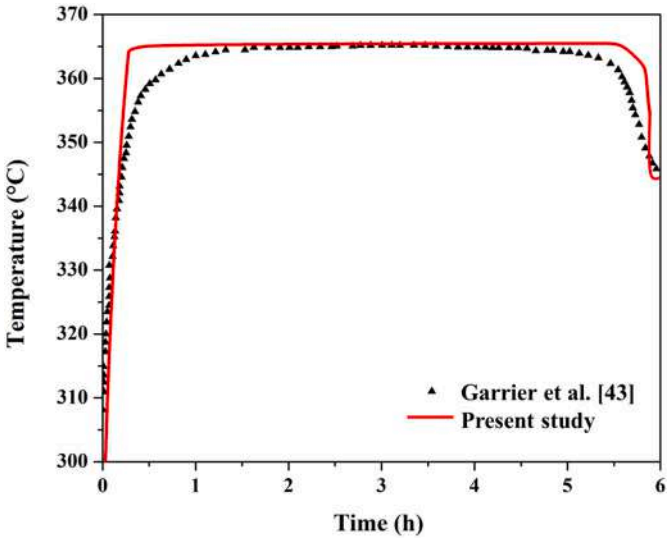

Fig. 5. Comparison between simulation and experimental result (Garrier et al. [43]).

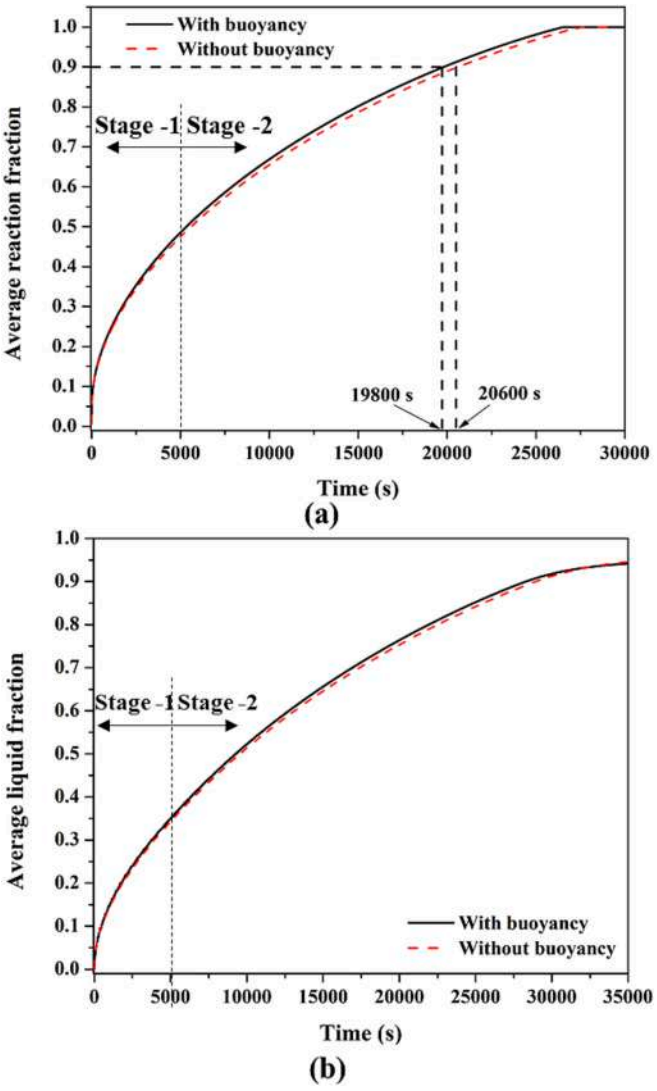

Fig. 6. Effect of buoyancy on average (a) reaction and (b) liquid fraction.

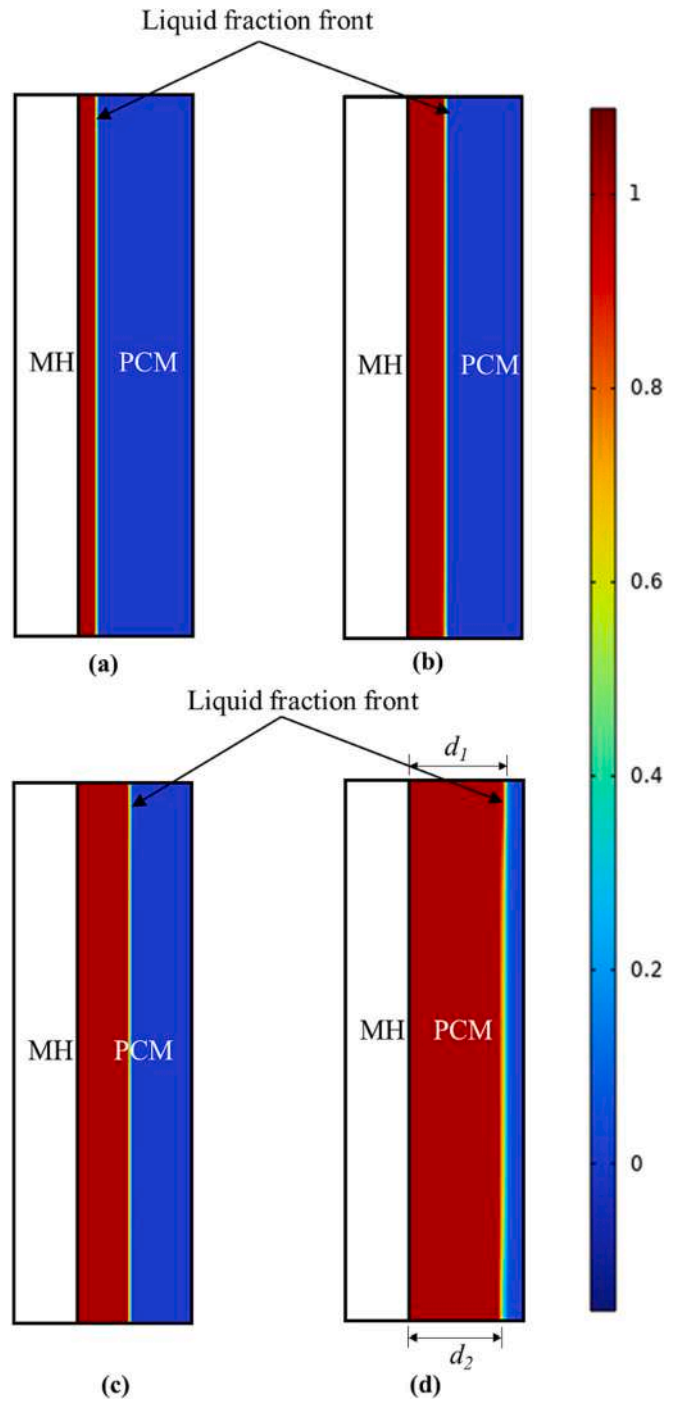

Fig. 7. Position of liquid fraction front with buoyancy at (a) 500 s, (b) 2000 s, (c) 5000 s and (d) 20,000 s.

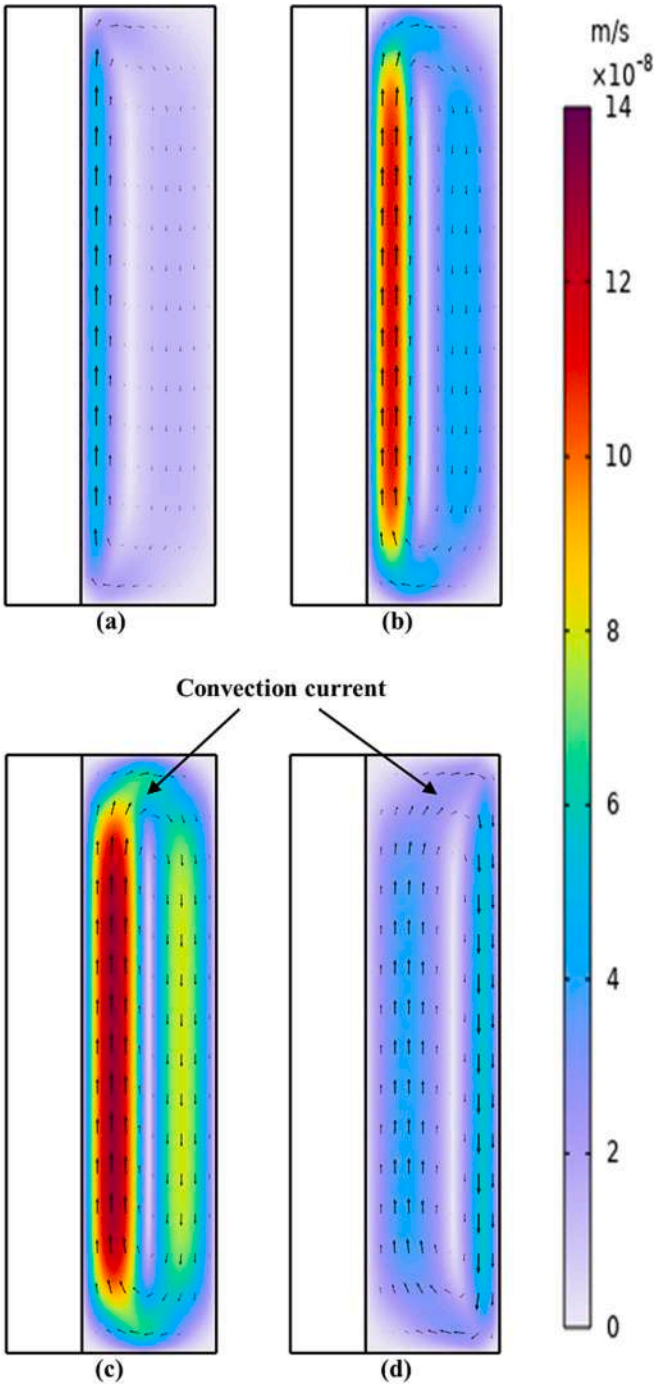

Fig. 8. Variation in velocity field in PCM at (a) 500 s, (b) 2000 s, (c) 5000 s and (d) 20,000 s.

which uses the finite element method. The user-defined functions are incorporated for the source term, reaction fraction, liquid fraction, etc. Before the detailed analysis, the model is validated against the experimental results presented by Garrier et al. [43]. The experimental work conducted by Garrier et al. [43] focused on investigating the hydrogen storage performance of a Mg MH reactor featuring $Mg_{69}Zn_{28}Al_3$ as the PCM. To verify the accuracy of the present mathematical model (using the equations outlined in Section 3), its results are compared with those reported by Garrier et al. [43] as shown in Fig. 5.

A slight deviation is noticeable at $t = 0.5$ h, and this can be attributed to certain simplifying assumptions adopted to facilitate the simulation as well as the use of approximated material properties in our current study. Nevertheless, it's important to emphasize that this observed deviation is relatively minor.

5.2. *Effect of buoyancy*

The reactor's geometry, operating conditions and properties of PCM and MH influence the buoyancy in the PCM domain. As PCM absorbs energy, it starts melting and the convection current sets in. Few studies [37,39] used the Navier-Stokes equation to solve this convection current. However, most of the other research [21,35,44,45] excluded this effect by neglecting convective heat transfer and considering only conduction due to the highly viscous nature of PCM.

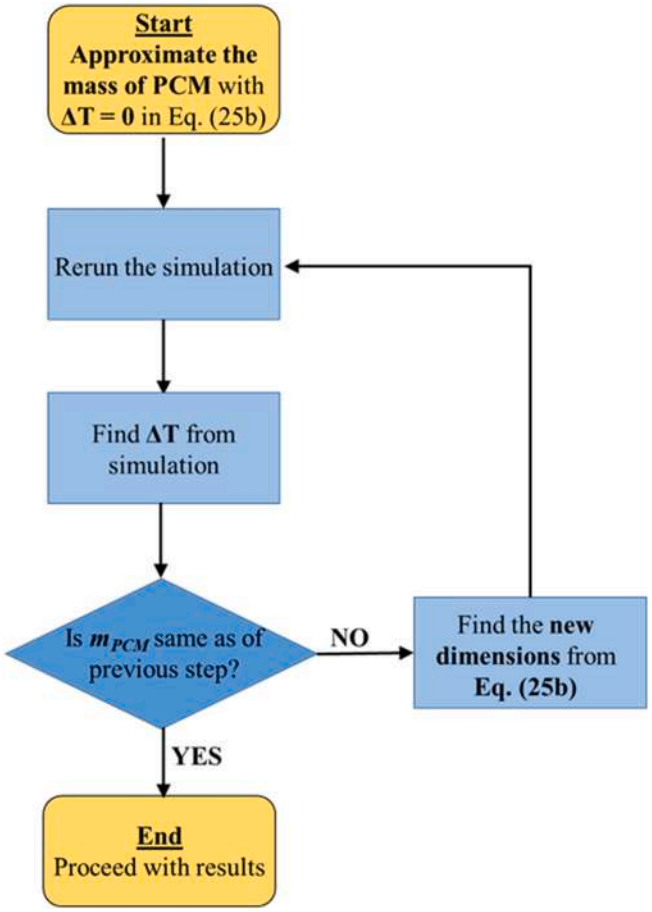

Fig. 9. Flowchart to estimate exact amount of PCM.

Bartolucci and Krastev [46] investigated the PCM melting rate in the $LaNi_5$ reactor with and without buoyancy effects. They reported that neglecting this effect may produce variations in outcomes up to 50 %. However, in the present work, the computational time to solve the model by considering the buoyancy effect (Navier-Stokes equation with Boussinesq approximation) is ~17 times more than without it. Hence, a proper investigation is required to understand the buoyancy effect.

Fig. 6(a) and (b) illustrate the effect of buoyancy on the average reaction fraction in MH and average liquid fraction in PCM, respectively. The hydrogen absorption and PCM melting are divided into Stages 1 and 2. The effect of buoyancy is insignificant in Stage 1, whereas in Stage 2, its effects are distinguishable compared to those without buoyancy. It is noticed from Fig. 6a that the time taken to achieve 90 % of hydrogen absorption is 19,800 and 20,600 s for with and without buoyancy, respectively. The formation of the convection current is significant in Stage 2 due to buoyancy, which improves the heat transfer from MH to PCM and leads to greater hydrogen absorption (Fig. 6a) and a faster melting rate (Fig. 6b).

Fig. 7 depicts the position of the liquid fraction front at various times. The liquid fraction of PCM increases with time, as observed in Fig. 7(a)–(d). In the latter, it can be observed that the liquid front is wider at the top than at the bottom ($d_1 > d_2$). This is because an increase in the convection current leads to greater PCM melting, resulting in an uneven distribution of liquid fraction at 20,000 s.

The variation in the velocity field and magnitude on the PCM side due to convection current is illustrated in Fig. 8(a)–(d). At 500 s, the formation of a convection current is not considerable due to the less liquefied region of PCM. However, it becomes significant with time and the amount of liquefied PCM. The velocity magnitude of PCM is more pronounced near the MH wall side (Fig. 8(a)–(c)) and later, it shifts

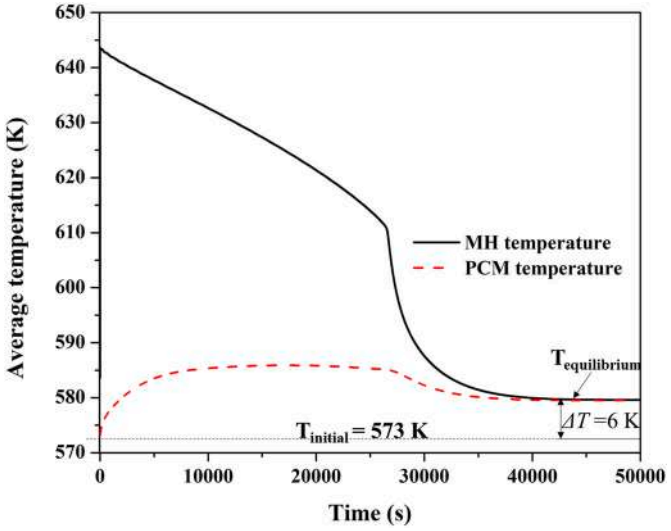

Fig. 10. Calculation of ΔT for the accurate mass of PCM.

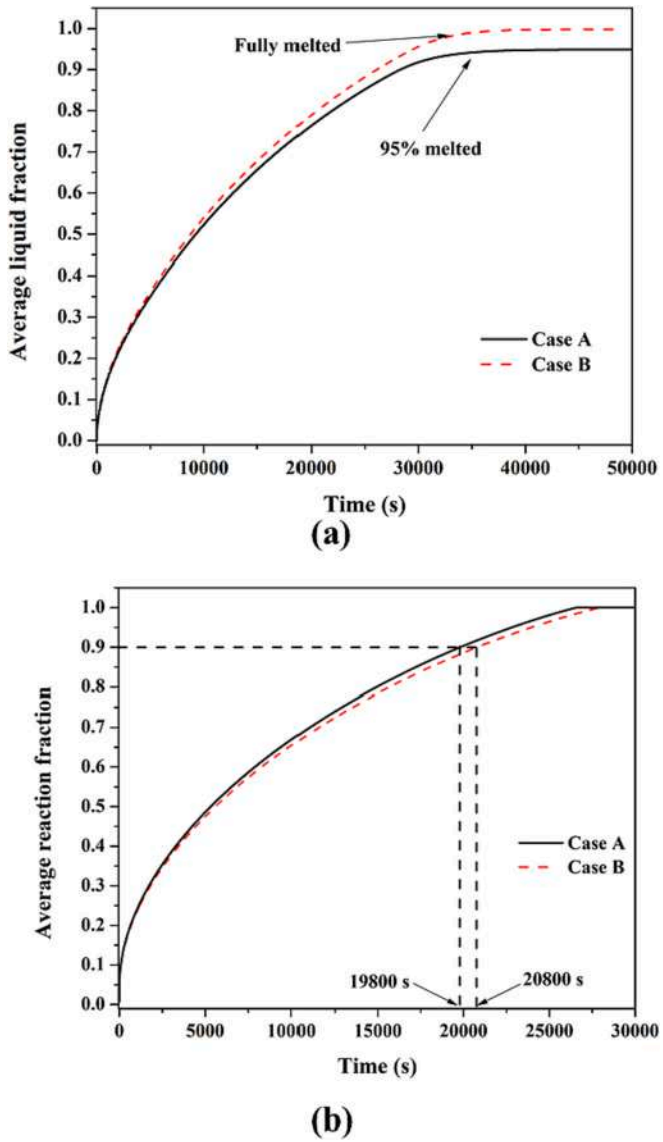

Fig. 11. Effect of amount of PCM average (a) liquid; and (b) reaction fraction.

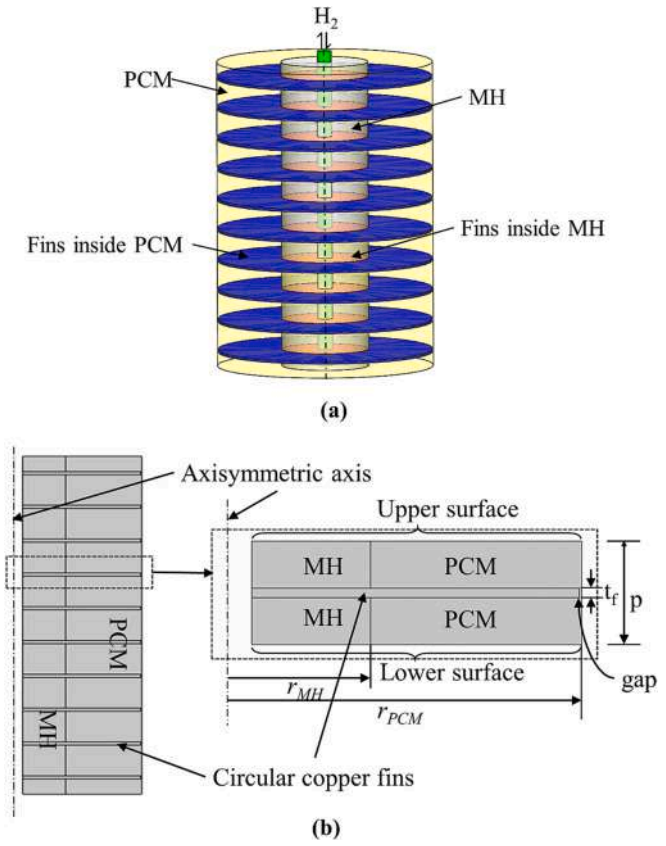

Fig. 12. MH reactor with fins and PCM (a) 3D view and (b) 2D computational domain used for simulation.

towards the PCM outer wall (Fig. 8d).

5.3. Amount of PCM

The system's overall weight and heat absorption capability depend on the mass of the PCM. Hence, the amount of PCM must be just enough to absorb the reaction heat released from MH. Some investigations [21,44,47] considered only the latent heat while estimating the amount of PCM. But sensible heat also plays an important role. Therefore, the present study evaluates the volume of the PCM required as follows:

$$E_{latent\ heat} + E_{sensible\ heat} = V_{MH} \cdot wt \cdot \rho_{MH} \cdot (1-\epsilon) \frac{\Delta H}{M_{H_2}} \tag{25a}$$

$$m_{PCM} = \frac{V_{MH} \cdot wt \cdot \rho_{MH} \cdot (1-\epsilon)\ \frac{\Delta H}{M_{H_2}}}{L + C_p(\Delta T)} \tag{25b}$$

The current investigation adopts the iterative technique shown in Fig. 9 as a flowchart to determine the exact amount of PCM required. The mass of PCM calculated without sensible heat ($\Delta T = 0$ in Eq. (25b)) is used as the initial guess for the first iteration. Then, the simulation is performed and the temperature difference ΔT (Fig. 10) associated with the sensible heat of PCM is calculated. New ΔT is introduced in Eq. (25b) to estimate the new mass of the PCM. The iteration is stopped when the mass of PCM from the present and previous steps are the same. The mass thus found is the accurate mass of PCM needed.

The variation of average liquid and reaction fractions with time for without (case A) and with (case B) sensible heat is demonstrated in Fig. 11(a) and (b), respectively. As case B dictates the exact amount of PCM needed to store the energy liberated from the reaction, it melts fully, whereas case A is 95 % melted (Fig. 11a). The hydrogen absorption of case A is better than case B due to more mass of PCM, as shown in

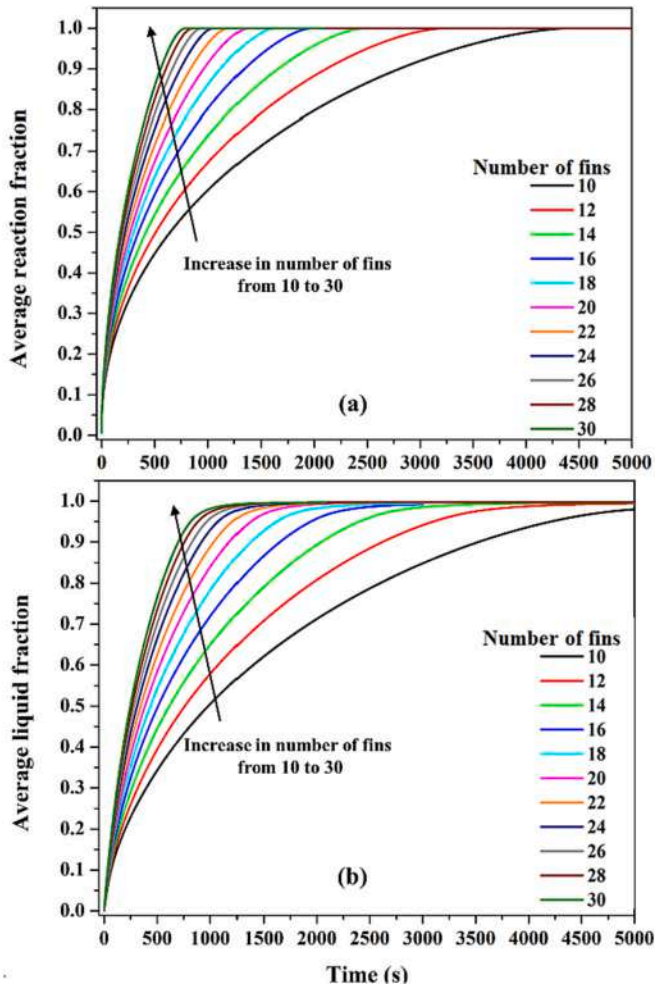

Fig. 13. Variation of average (a) reaction and (b) liquid fraction with time for different number of fins.

Fig. 11b. Cases A and B require 19,800 and 20,800 s to absorb 90 % of the hydrogen, respectively.

Case B takes 4.7 % more time than case A, but the latter is heavier than the former by 6.7 %. The improvement in hydrogen absorption rate is less than the increment in the system's weight when sensible energy is neglected. Therefore, the present study considers both the sensible and latent heat (Eq. (25b)) to determine the accurate mass of PCM, which will be used for further investigations.

5.4. Effect of fins

Several studies [19,31,48,49] in the literature used the fins as an extended surface to improve heat transfer and hence reactor performance. In the present study, due to the poor thermal conductivity of both MH and PCM, the circular copper fins are incorporated inside the reactor to enhance the heat transfer from MH to PCM and vice versa (Fig. 12a).

5.4.1. Fin addition

Fig. 12b presents the computational domain of the 2D axisymmetric model. Due to the reactor's periodic symmetry, only one part is considered for simulation, whose height corresponds to the pitch (p). The PCM melting initiates the formation of convection currents, which result in the distinction between the upper and lower surface. Henceforth, periodic boundary conditions are imposed upon both the upper and lower surfaces to govern the processes of heat and mass transfer.

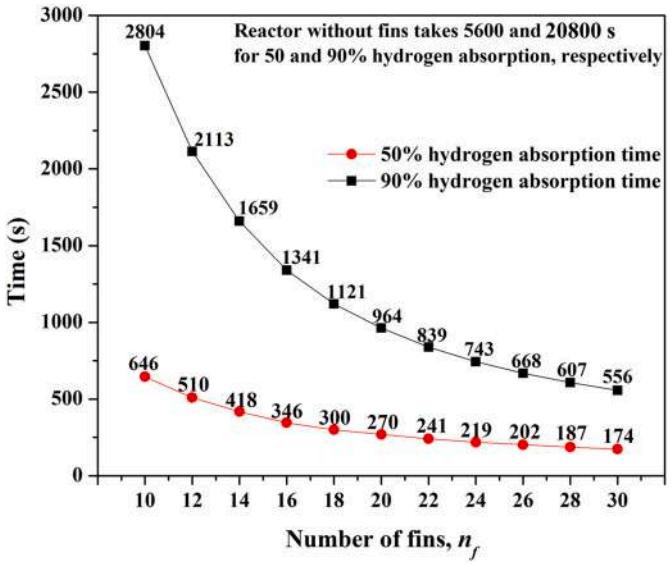

Fig. 14. Variation in time for 50 and 90 % of hydrogen absorption with number of fins.

These conditions are defined as follows:

$$-\boldsymbol{q}_{low}\cdot\boldsymbol{n}_{low} = \boldsymbol{q}_{up}\cdot\boldsymbol{n}_{up} \tag{26}$$

where $\boldsymbol{q}_{low}$ and the $\boldsymbol{q}_{up}$ denote the flux (heat, mass and concentration flux) from the lower surface and upper surface, respectively and $\boldsymbol{n}_{low}$ and $\boldsymbol{n}_{up}$ is the respective area unit vector.

A minimal radial gap known as tip clearance of 0.5 mm is maintained between the fin and the PCM outer wall to improve convection circulation between the top and bottom layers of the PCM [50]. The number of fins is varied from 10 to 30, keeping the total mass of the fins constant (1 kg) by altering the fin thickness (t_f) and pitch (p) accordingly. Thus, t_f and p work out to be 2 and 21.92 mm, respectively, for 10 fins and 1 and 10.96 mm for 20 fins.

Adding more fins increases the contact surface area between the MH and PCM for efficient heat transfer, which induces better hydrogen absorption and liquid fraction rates, as depicted in Fig. 13(a) and (b), respectively. The increase in the number of fins decreases the corresponding pitch, reducing the domain of MH and leading to proportionately less energy generation per fin. As a result, the heat transfer duty of every fin decreases with the marginal increase in thermal resistance of the fin (due to reduction in t_f). Hence, the hydrogen absorption time reduces with an increase in the number of fins. Similarly, liquid fraction also follows the same trend.

Fig. 14 demonstrates the effect of the number of fins on time taken for 50 and 90 % hydrogen absorption. It is observed that the time decreases with an increase in the number of fins, but the decrement becomes insignificant beyond 28 fins. This is due to a corresponding reduction in the fin thickness and a trivial decrease in fin pitch (i.e., associated MH per fin). Further, an increased number of fins leads to greater manufacturing complexities. Therefore, 28 fins are considered ideal and are taken up for further investigation.

The effect of fins on local liquid fraction at various times is illustrated in Fig. 15. The liquid fraction front progresses more radially and longitudinally with the increase in the number of fins. A careful observation of the case having 10 fins reveals that the progression of the fraction front follows the U pattern, whereas other cases follow the V pattern. The internal angle widens with the increase in fins, enhancing the heat transfer from the fin to PCM relative to the MH-PCM interface area. In the system with 28 fins, heat transfer from the fin surface is more significant than in the system with 10 fins.

5.4.2. Fin efficiency and fin factor

The η_f is defined as the ratio of the actual heat transfer rate ($\dot{Q}$) to the maximum heat transfer rate when the whole fin is at base temperature ($\dot{Q}_{max}$). Conventionally, the driving potential is the temperature difference between the fin and the surrounding fluid (which is constant) in a steady state.

In the present study, temperature profiles of fin and MH are used to estimate η_f. The fin is exposed to MH medium with transient heat transfer as against air medium with steady heat transfer in the conventional case. Further, the temperature of the former not only varies with spatial dimensions (r, z) but also with time, $T_{MH} = T(r, z, t)$, unlike

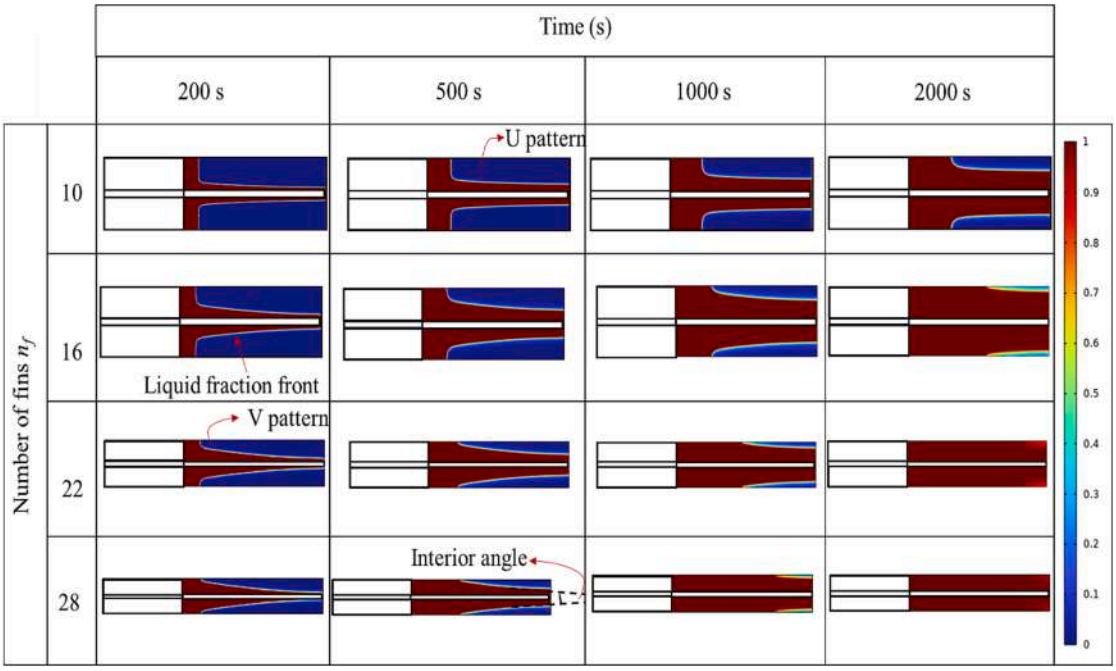

Fig. 15. Effect of fins on local liquid fraction at various times.

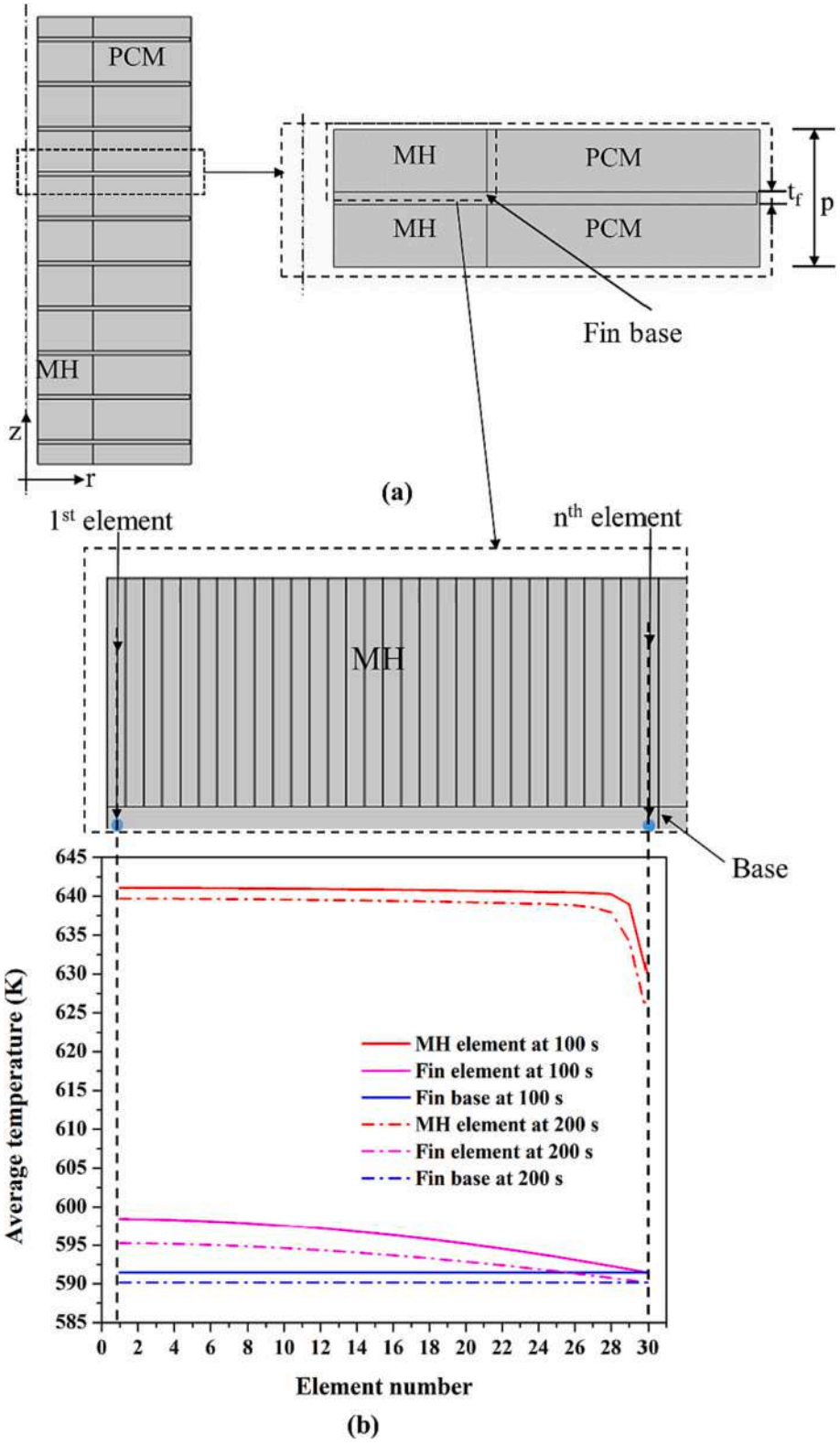

Fig. 16. Schematic of (a) 2D computational domain and (b) variation of average temperature with number of elements.

the latter. In addition, the fin base temperature is also time-dependent.

The η_f is determined for the fins on the MH side since the primary concern of the present study is to improve the hydrogenation rate. Fig. 16b presents the discretization of the MH domain into small sub-domains. For the present case, MH is divided into 30 sub-domains known as elements. The average temperature distribution of the elements varies only radially and not longitudinally, $T_{MHavg} = T(r, t)$. The copper fins have high thermal conductivity, so the temperature gradient in the z direction will be negligible inside them. Thus, their temperature distribution is purely radial, $T_{fin} = T(r, t)$. Therefore, the fin is not discretized. However, the temperature of the points in the fin corresponding to MH elements is determined.

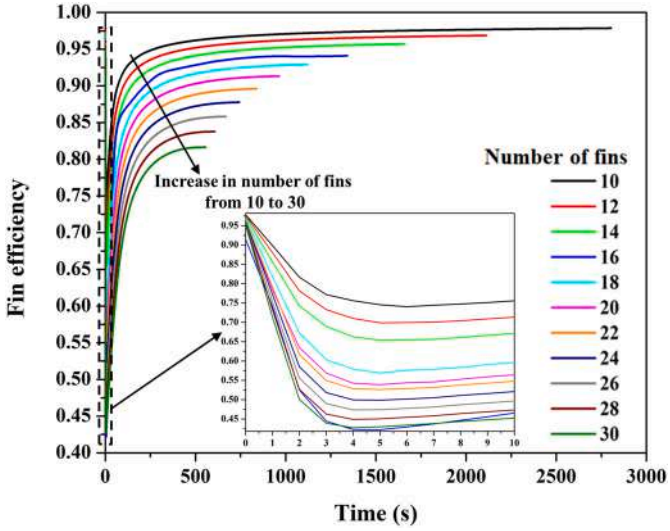

Fig. 17. Fin efficiency for various number of fins.

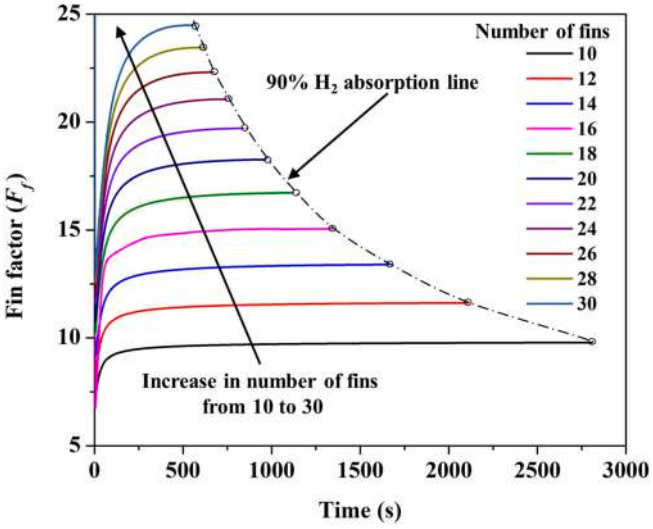

Fig. 18. Variation of fin factor with time for different number of fins.

Furthermore, Fig. 16b presents the variation of average MH, fin and the base temperature with the number of elements. The temperature of MH elements rises due to exothermic reaction; as a result, initially, these elements don't have a temperature gradient along the radial direction. However, the 30th element is in immediate contact with PCM, which is at a lower temperature. Due to this, a temperature gradient exists between them. Hence, the temperature of the last elements is comparatively less. In addition, the fin temperature profile is smooth and decreases from the 1st to the 30th element. For the maximum heat transfer $\dot{Q}_{max}$, the fin temperature of the 30th element is considered the base temperature (producing the maximum driving potential) and is a spatial constant.

Heat transfer across any particular element is due to the temperature gradient between the respective fin and the MH element. Like conventional heat exchanger cases where fluid temperature varies along the direction of flow, similarly, in the present context, the temperature of MH and fin varies radially. Therefore, the LMTD approach is employed in this analysis. Thus, the total heat transfer $(\dot{Q})$ is given by Eq. (27).

$$\dot{Q} = U{\cdot}A{\cdot}LMTD \tag{27}$$

where U is the overall heat transfer coefficient [W m^{-2} K^{-1}], A is the contact surface area [m^2] and LMTD is defined by Eq. (28).

$$LMTD = \frac{\left(T_{MH1} - T_{f1}\right) - \left(T_{MH30} - T_{f30}\right)}{ln\left(\frac{T_{MH1} - T_{f1}}{T_{MH30} - T_{f30}}\right)} \tag{28}$$

where, T_{MH1} *and* T_{MH30} denotes the temperature of the 1st and 30th element of the MH, respectively. T_{f1} *and* T_{f30} denotes the temperature of the 1st and 30th point in the fin corresponding to the 1st and 30th element of the MH, respectively.

But for any particular system with a defined number of fins, U and A are constant; thereby, η_f in terms of LMTD can be evaluated by Eq. (29).

$$\eta_f = \frac{\dot{Q}_{act}}{\dot{Q}_{max}} = \frac{(U{\cdot}A{\cdot}LMTD)_{act}}{(U{\cdot}A{\cdot}LMTD)_{max}} = \frac{(LMTD)_{act}}{(LMTD)_{max}} \tag{29}$$

Fig. 17 displays the η_f with time for various numbers of fins up to 90 % hydrogen absorption. During the initial period, the η_f is very high for all the cases due to the initiation of the exothermic reaction. In this period, the heat is not transferred to the fin from MH (due to poor k_{MH}). Hence, the whole fin is at the same temperature resembling the ideal nature. However, the heat starts transferring with time, resulting in the non-uniform temperature distribution of the fin (Fig. 16b). The η_f of the system having 10 fins is always superior to others due to the increase in their thickness.

For fin optimization, both η_f and the mass of MH are considered since the heat transmitted from MH to the fin depends on the reaction heat liberated. With the increase in the number of fins, the MH associated with the fin decreases due to a reduction in pitch. Therefore, a new non-dimensional parameter called the "fin factor (F_f)" is introduced as follows.

$$F_f = \eta_f \times \frac{total\ mass\ of\ MH}{mass\ of\ MH\ available\ for\ fin} \tag{30}$$

Fig. 18 shows the variation of F_f with time for different numbers of fins up to 90 % hydrogen absorption. At any instant, F_f is higher for more number of fins. As displayed before in Fig. 17, the η_f increases with the decrease in the number of fins, but the heat transfer duty of the fin reduces due to the reduction in volumetric energy generation in MH and the reduction in the latter is more significant than the increment of the former.

The parameter F_f gives a better picture of optimizing the number of fins compared to the η_f as it provides a better notion of heat transfer from the fin compared to the heat available. F_f for the reactor with 28 and 30

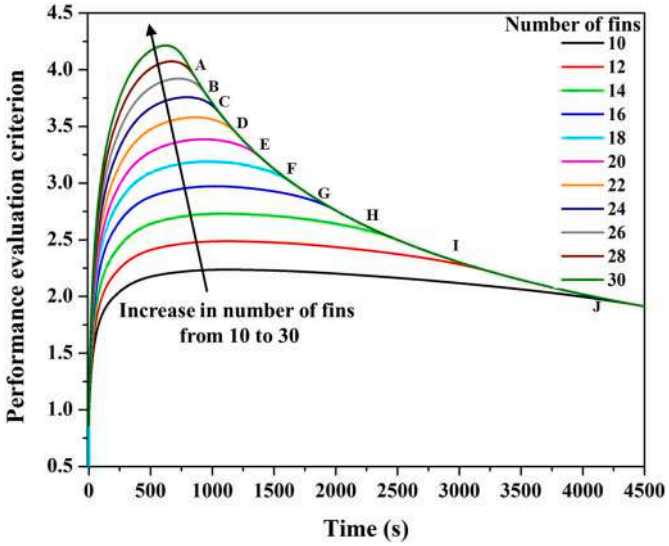

Fig. 19. Variation of PEC with different number of fins.

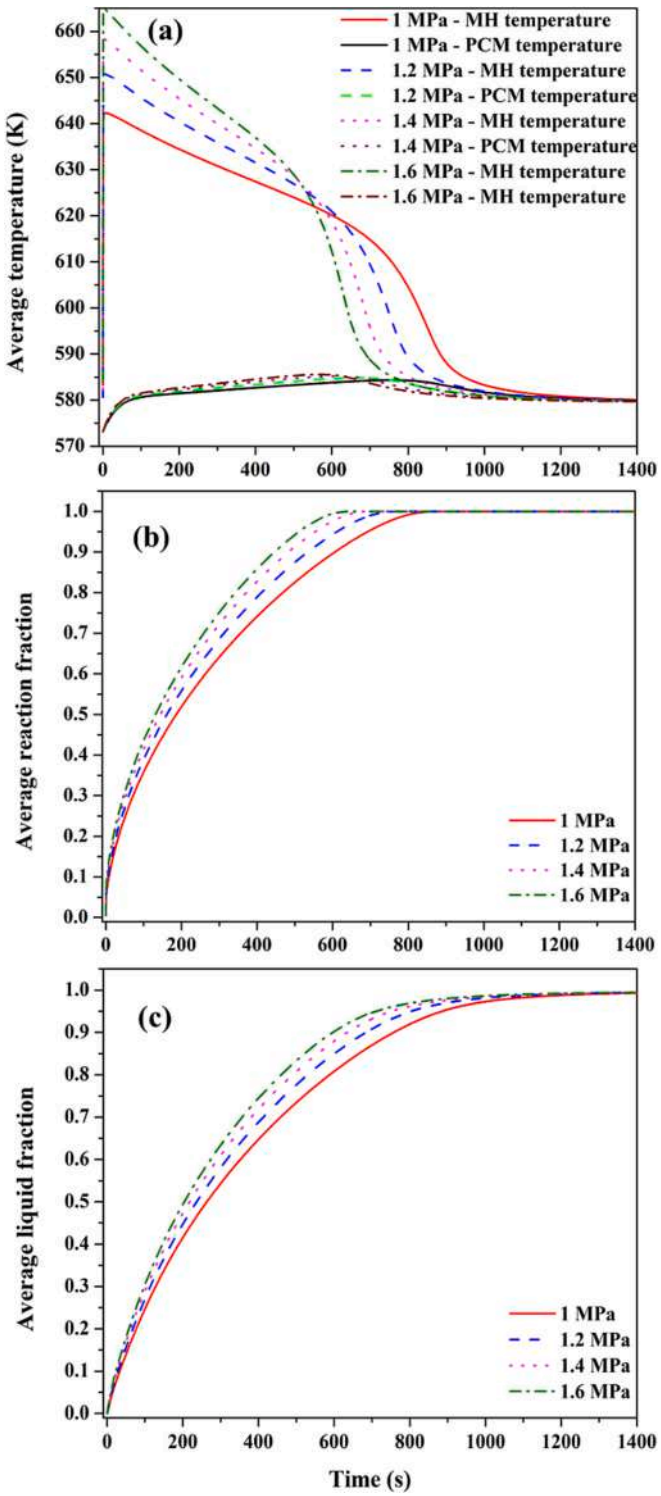

Fig. 20. Effect of hydrogen supply pressure on average (a) temperature, (b) reaction fraction and (c) liquid fraction.

fins are nearly the same. Therefore, optimizing both the hydrogen absorption rate and F_f and reducing the manufacturing complexities, the reactor with 28 fins is considered for further investigation.

5.5. Performance evaluation criterion

Adding fins increases the heat transfer at the cost of the system's overall weight. A non-dimensionless parameter called performance evaluation criterion (PEC) is proposed as the ratio of two dimensionless factors and is defined by Eq. (31). It is the relative measure of merit (increase in ab/desorption rate) and demerit (increase in the weight of the system) of having fins.

$$PEC = \frac{\text{Hydrogen absorption with fins}/\text{Hydrogen absorption without fins}}{\text{System weight with fins}/\text{System weight without fins}} \tag{31}$$

The PEC variation with the time for different fin numbers is demonstrated in Fig. 19. The peak point in every PEC curve signifies the system's best performance with respect to the system without fin at that instant. All the PEC curves for different fin numbers intersect at points denoted by A to J. The curve in the region before these merging points shows the superiority of having more fins. In contrast, after these points, the importance of having more fins is in vain. Higher PEC values indicate better heat and mass transfer in MH reactors.

5.6. Effect of operating conditions

5.6.1. Hydrogen supply pressure

The hydrogen supply pressure is one of the essential operating parameters since the reaction kinetics depend very much on it. The pressure differential (the difference between supply and equilibrium pressure) drives the mass transfer. Eq. (5) suggests that the heat source term increases with the supply pressure, which results in the sudden rise of MH temperature (Fig. 20a).

The supply pressure for the reactor with 28 fins is varied from 1 to 1.6 MPa. The peak temperatures of 642.27, 650.83, 658.25 and 664.81 K correspond to absorption pressures 1, 1.2, 1.4 and 1.6 MPa, respectively. The increase in temperature of MH produces the high-temperature gradient between MH and PCM, causing more significant heat transfer and leading to the rise in hydrogen absorption and liquid fraction rates, as observed in Fig. 20(b) and (c), respectively. The supply pressure of 1, 1.2, 1.4 and 1.6 MPa takes 607, 535, 484 and 447 s, respectively, for 90 % hydrogen absorption. The increase in supply pressure creates a higher temperature differential between MH and PCM, leading to an increased PCM melting rate.

5.6.2. Initial temperature

In energy storage applications, the PCMs are used to take advantage of their high latent enthalpy [51]. Every PCM has a specified melting temperature, and the amount of energy stored in PCM as latent and sensible heat thus depends on the operating temperature conditions.

To study the effect of initial temperature on the system's performance, the initial temperatures T_1, T_2 and T_3 are considered as Cases 1, 2 and 3, respectively, and their values are defined by Eqs. (32a), (32b), and (32c). The initial sensible heat in Case 1 is more than Case 2, whereas it is nil for Case 3.

$$T_1 = T_0 \tag{32a}$$

$$T_2 = \frac{T_1 + T_{sol}}{2} \tag{32b}$$

$$T_3 = T_{sol} \tag{32c}$$

where T_0 is the initial temperature defined earlier as 300 °C and T_{sol} is the solid phase transition temperature of the PCM.

Fig. 21a demonstrates the variation of an average liquid fraction with time. The time taken for the complete melting of PCM for Cases 1, 2 and 3 is 1686, 1142 and 964 s, respectively. Notably, the PCM in Case 3 melts very quickly compared to the others. This is due to the initial temperature of PCM being equal to the solid phase temperature, thereby absorbing latent heat first. In contrast, the others absorb sensible and then latent heat.

Fig. 21b depicts the effect of initial temperature on the average

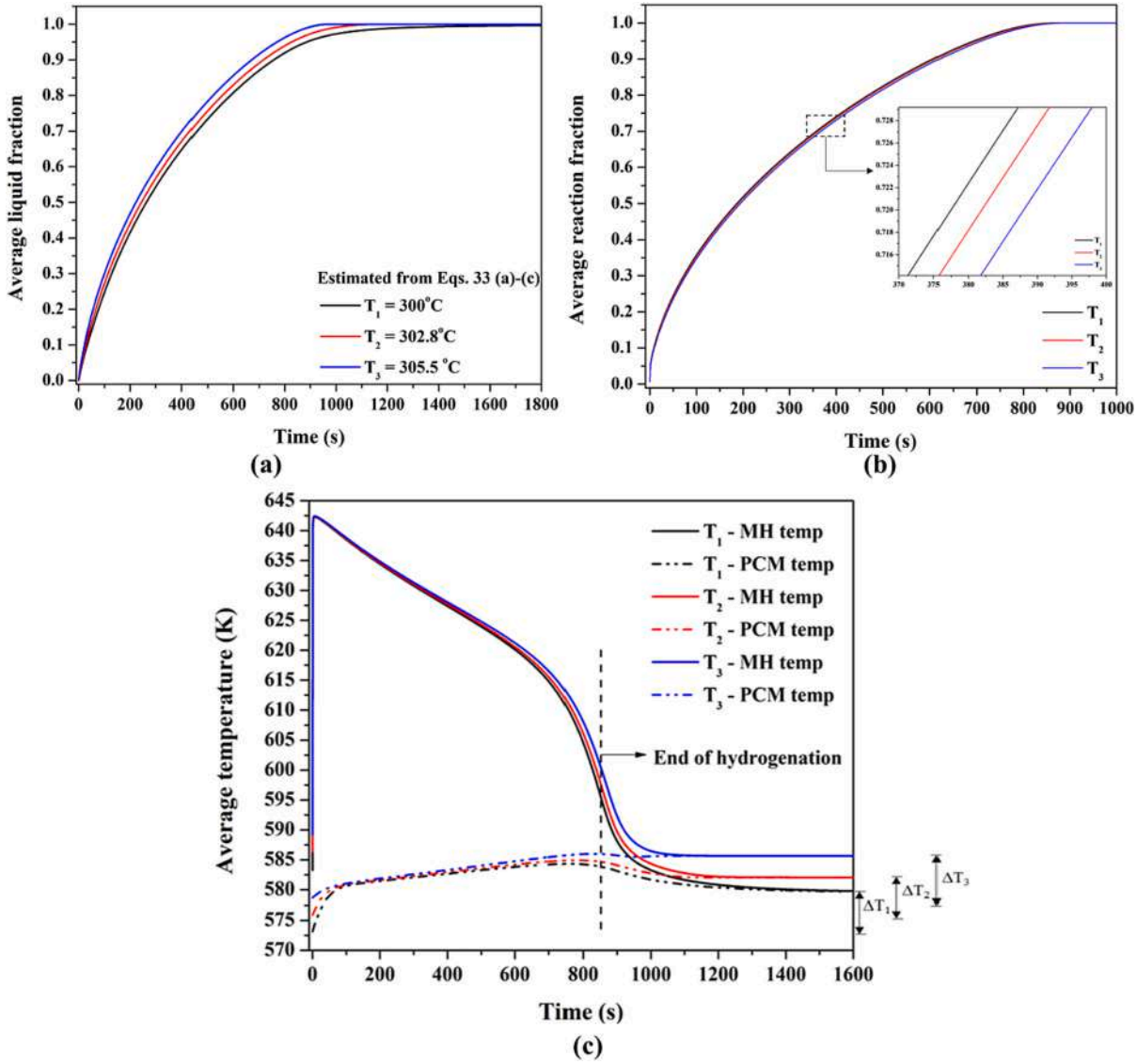

Fig. 21. Effect of initial temperature on average (a) liquid fraction, (b) reaction fraction and (c) temperature.

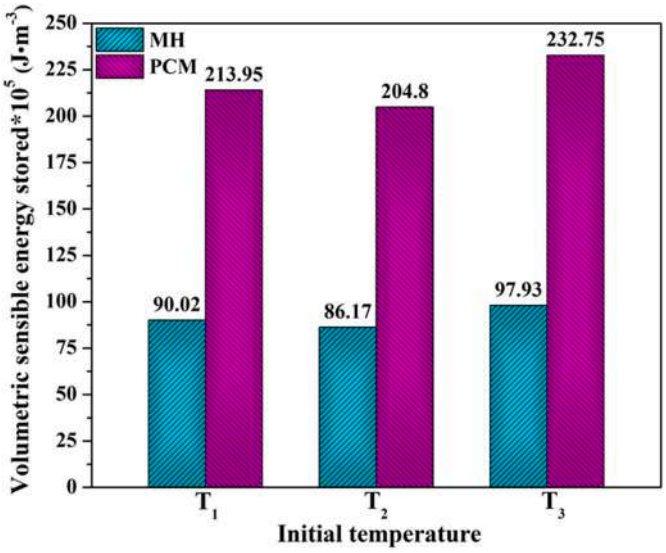

Fig. 22. Comparison of volumetric sensible heat storage for MH and PCM.

reaction fraction with time. The reaction fraction of Case 1 is more rapid than in other cases, but this deviation is not much significant. Therefore, the average reaction fraction is less sensitive to the initial temperature.

The variation in the average temperature of MH and PCM is illustrated in Fig. 21c. A sharp dip is observed in the MH temperature profile of all the cases due to complete hydrogenation. The final equilibrium temperature of the system for Cases 1, 2 and 3 are 579.6, 582 and 585.6 K, respectively, corresponding to PCM temperature change as $\Delta T_1 = 6.4$, $\Delta T_2 = 6.1$, and $\Delta T_3 = 6.95$ K.

Fig. 21a illustrates that the whole PCM is melted in all cases. Therefore, the amount of latent heat stored in PCM is the same in all cases and is equal to 3578.69×10^5 J·m^{-3}.

$$Volumetric\ sensible\ heat\ stored_{MH/PCM} = (\rho C_P \cdot \Delta T)_{MH/PCM} \quad (33)$$

Eq. (33) estimates the sensible heat stored in MH or PCM. Fig. 22 denotes the volumetric sensible heat stored in MH and PCM for various initial temperatures. PCM's sensible heat storage is higher than MH due to its greater volumetric specific heat capacity (ρC_p). It is worth noting that the minimum ratio of latent to sensible heat stored for the present PCM is nearly 15.4. Therefore, the maximum amount of energy is stored as latent heat in PCM.

6. Conclusions

The present study numerically investigated a 2D axisymmetric model of MH reactor surrounding PCM. The buoyancy effects should be considered in a hydrogen storage reactor with PCM. η_f, F_f and PEC are proposed based on obtained results. The salient conclusions from the present research are made:

- The buoyancy effect generates convection currents, thereby improving heat transfer and the melting rate of PCM, resulting in a ~4 % reduction in the time required to achieve 90 % hydrogen absorption.
- The suggested iterative method estimates around 6.7 % less PCM mass compared to the conventional method.
- The reactor achieves 50 and 90 % hydrogen absorption in 5600 and 20,800 s, respectively, when no fins are present.
- The reactor with 28 fins takes ~97 % less time than the reactor with 10 fins to achieve 90 % hydrogen absorption.
- The F_f is a better parameter to optimize the hydrogen storage reactor as compared to the η_f. The highest F_f value of 24.5 is observed for a reactor with 30 fins at 556 s for 90 % hydrogen absorption.
- PEC increases with the number of fins. The maximum and minimum PEC values of 4.2 and 2.2 were noticed for 30 and 10 fins, respectively.
- The increase in supply pressure has a more significant effect on hydrogen absorption compared to the initial temperature of the reactor. The maximum and minimum supply pressure of 1.6 and 1 MPa takes 447 and 607 s, respectively for 90 % hydrogen absorption.
- Case 1 requires an additional time of 544 and 722 s for the complete melting of PCM compared to Cases 2 and 3, respectively.

CRediT authorship contribution statement

Ankush Parmanand Shrivastav: Conceptualization, Methodology, Software, Validation, Data curation, Writing – review & editing, Visualization. **Praveen Kumar Kanti:** Conceptualization, Methodology, Data curation, Formal analysis, Investigation, Writing – review & editing, Visualization. **G. Mohan:** Formal analysis, Visualization, Writing – review & editing. **M.P. Maiya:** Conceptualization, Methodology, Data curation, Writing – review & editing, Investigation, Resources, Visualization, Supervision, Project administration.

Declaration of competing interest

The authors declare that they have no known competing financial interests or personal relationships that could have appeared to influence the work reported in this paper.

Data availability

Data will be made available on request.

Acknowledgment

The authors would like to express their gratitude to the Department of Science and Technology, New Delhi, Government of India, vide Grant Number: DST/TMD/MECSP/2K17/50 (G).

References

[1] T. Ahmad, D. Zhang, A critical review of comparative global historical energy consumption and future demand: the story told so far, Energy Rep. 6 (2020) 1973–1991, https://doi.org/10.1016/j.egyr.2020.07.020.
[2] J. Yao, P. Zhu, L. Guo, L. Duan, Z. Zhang, S. Kurko, Z. Wu, A continuous hydrogen absorption/desorption model for metal hydride reactor coupled with PCM as heat management and its application in the fuel cell power system, Int. J. Hydrogen Energy 45 (52) (2020) 28087–28099, https://doi.org/10.1016/j.ijhydene.2020.05.089.
[3] B. Acikgoz, C. Celik, An experimental study on performance and emission characteristics of a methane–hydrogen fuelled gasoline engine, Int. J. Hydrogen Energy 37 (23) (2012) 18492–18497, https://doi.org/10.1016/j.ijhydene.2012.09.037.
[4] C. Ronneau, Energie, pollution de l'air et d'eveloppement durable, Presses univ. de Louvain, 2013.
[5] P.K. Kanti, A.P. Shrivastav, P. Sharma, M. Maiya, Thermal performance enhancement of metal hydride reactor for hydrogen storage with graphene oxide nanofluid: model prediction with machine learning, Int. J. Hydrogen Energy (2023), https://doi.org/10.1016/j.ijhydene.2023.03.361.
[6] P. Muthukumar, M. Prakash Maiya, S. Srinivasa Murthy, Experiments on a metal hydride based hydrogen compressor, Int. J. Hydrogen Energy 30 (8) (2005) 879–892, https://doi.org/10.1016/j.ijhydene.2004.09.003.
[7] S. Anbarasu, P. Muthukumar, S.C. Mishra, Thermal modeling of Mg_2Ni based solid-state hydrogen storage reactor, Heat Transfer Eng. 35 (14–15) (2014) 1354–1362, https://doi.org/10.1080/01457632.2013.877314.
[8] I. Jain, C. Lal, A. Jain, Hydrogen storage in Mg: a most promising material, Int. J. Hydrogen Energy 35 (10) (2010) 5133–5144, https://doi.org/10.1016/j.ijhydene.2009.08.088.
[9] S. Mellouli, F. Askri, H. Dhaou, A. Jemni, S. Ben Nasrallah, A novel design of a heat exchanger for a metal-hydrogen reactor, Int. J. Hydrogen Energy 32 (15) (2007) 3501–3507, https://doi.org/10.1016/j.ijhydene.2007.02.039.
[10] S. Mellouli, F. Askri, H. Dhaou, A. Jemni, S. Ben Nasrallah, Numerical study of heat exchanger effects on charge/discharge times of metal–hydrogen storage vessel, Int. J. Hydrogen Energy 34 (7) (2009) 3005–3017, https://doi.org/10.1016/j.ijhydene.2008.12.099.
[11] F. Askri, M. Ben Salah, A. Jemni, S. Ben Nasrallah, Optimization of hydrogen storage in metal-hydride tanks, Int. J. Hydrogen Energy 34 (2) (2009) 897–905, https://doi.org/10.1016/j.ijhydene.2008.11.021.
[12] Y. Kaplan, Effect of design parameters on enhancement of hydrogen charging in metal hydride reactors, Int. J. Hydrogen Energy 34 (5) (2009) 2288–2294, https://doi.org/10.1016/j.ijhydene.2008.12.096.
[13] J. Sunku Prasad, P. Muthukumar, Experimental investigation on annular metal hydride reactor for medium to large-scale hydrogen storage applications, Journal of Energy Storage 44 (2021) 103473, https://doi.org/10.1016/j.est.2021.103473.
[14] M.-L. Tsai, T.-S. Yang, On the selection of metal foam volume fraction for hydriding time minimization of metal hydride reactors, Int. J. Hydrogen Energy 35 (20) (2010) 11052–11063, https://doi.org/10.1016/j.ijhydene.2010.07.081.
[15] F. Laurencelle, J. Goyette, Simulation of heat transfer in a metal hydride reactor with aluminium foam, Int. J. Hydrogen Energy 32 (14) (2007) 2957–2964, https://doi.org/10.1016/j.ijhydene.2006.12.007.
[16] S. Ferekh, G. Gwak, S. Kyoung, H. goo Kang, M. ho Chang, S. hun Yun, Y. hee Oh, W. Kim, D. Kim, T. Hong, H. Ju, Numerical comparison of heat-fin- and metal-foam-based hydrogen storage beds during hydrogen charging process, Int. J. Hydrogen Energy 40 (42) (2015) 14540–14550, https://doi.org/10.1016/j.ijhydene.2015.07.149.
[17] L. Tong, J. Xiao, P. B'enard, R. Chahine, Thermal management of metal hydride hydrogen storage reservoir using phase change materials, Int. J. Hydrogen Energy 44 (38) (2019) 21055–21066, https://doi.org/10.1016/j.ijhydene.2019.03.127.
[18] H. Ben Mâad, A. Miled, F. Askri, S. Ben Nasrallah, Numerical simulation of absorption-desorption cyclic processes for metal-hydrogen reactor with heat recovery using phase-change material, Appl. Therm. Eng. 96 (2016) 267–276, https://doi.org/10.1016/j.applthermaleng.2015.11.093.
[19] X.-S. Bai, W.-W. Yang, X.-Y. Tang, Z.-Q. Dai, F.-S. Yang, Parametric optimization of coupled fin-metal foam metal hydride bed towards enhanced hydrogen absorption performance of metal hydride hydrogen storage device, Energy 243 (2022), 123044, https://doi.org/10.1016/j.energy.2021.123044.
[20] Y. Zhuo, S. Jung, Y. Shen, Numerical study of hydrogen desorption in an innovative metal hydride hydrogen storage tank, Energy Fuel 35 (13) (2021) 10908–10917, https://doi.org/10.1021/acs.energyfuels.1c00666.
[21] T. Alqahtani, A. Bamasag, S. Mellouli, F. Askri, P.E. Phelan, Cyclic behaviors of a novel design of a metal hydride reactor encircled by cascaded phase change materials, Int. J. Hydrogen Energy 45 (56) (2020) 32285–32297, https://doi.org/10.1016/j.ijhydene.2020.08.280.
[22] H. Ben Mâad, F. Askri, J. Virgone, S. Ben Nasrallah, Numerical study of high temperature metal-hydrogen reactor (Mg_2Ni-H_2) with heat reaction recovery using phase-change material during desorption, Appl. Therm. Eng. 140 (2018) 225–234, https://doi.org/10.1016/j.applthermaleng.2018.05.009.
[23] A. Aadhithiyan, K. Bhargav, R. Sreeraj, S. Anbarasu, Multi-objective design optimization of hydride hydrogen storage reactor structured with finned helical tubes based on energetic and economic analyses, Journal of Energy Storage 64 (2023), 107194, https://doi.org/10.1016/j.est.2023.107194.
[24] K. Venkata Krishna, Praveen Kumar Kanti, M.P. Maiya, A novel fin efficiency concept to optimize solid state hydrogen storage reactor, Energy 288 (2024), 129789, https://doi.org/10.1016/j.energy.2023.129789.
[25] M. Afzal, N. Sharma, N. Gupta, P. Sharma, Transient simulation studies on a metal hydride based hydrogen storage reactor with longitudinal fins, Journal of Energy Storage 51 (2022), 104426, https://doi.org/10.1016/j.est.2022.104426.
[26] X.-S. Bai, W.-W. Yang, Y.-J. Yang, K.-R. Zhang, F.-S. Yang, Multivariable optimization of metal hydride hydrogen storage reactor with gradient porosity metal foam and evaluation of comprehensive performance, Int. J. Hydrogen Energy 47 (83) (2022) 35340–35351, https://doi.org/10.1016/j.ijhydene.2022.08.123.

[27] V. Arumuru, K. Rajput, R. Nandan, P. Rath, M. Das, A novel synthetic jet based heat sink with PCM filled cylindrical fins for efficient electronic cooling, Journal of Energy Storage 58 (2023), 106376, https://doi.org/10.1016/j.est.2022.106376.
[28] A.A.R. Darzi, H.H. Afrouzi, A. Moshfegh, M. Farhadi, Absorption and desorption of hydrogen in long metal hydride tank equipped with phase change material jacket, Int. J. Hydrog. Energy 41 (2016) 9595–9610.
[29] A. Chibani, S. Merouani, C. Bougriou, The performance of hydrogen desorption from a metal hydride with heat supply by a phase change material incorporated in porous media (metal foam): heat and mass transfer assessment, Journal of Energy Storage 51 (2022), 104449, https://doi.org/10.1016/j.est.2022.104449.
[30] H.Q. Nguyen, M. Mourshed, B. Paul, B. Shabani, An experimental study of employing organic phase change material for thermal management of metal hydride hydrogen storage, Journal of Energy Storage 55 (2022), 105457, https://doi.org/10.1016/j.est.2022.105457.
[31] Y. Ye, J. Lu, J. Ding, W. Wang, J. Yan, Numerical simulation on the storage performance of a phase change materials based metal hydride hydrogen storage tank, Appl. Energy 278 (2020), 115682, https://doi.org/10.1016/j.apenergy.2020.115682.
[32] A. Chaise, P. Marty, P. de Rango, D. Fruchart, A simple criterion for estimating the effect of pressure gradients during hydrogen absorption in a hydride reactor, International Journal of Heat and Mass Transfer 52 (19) (2009) 4564–4572, https://doi.org/10.1016/j.ijheatmasstransfer.2009.03.052.
[33] M. Bhouri, I. Bürger, Numerical investigation of H2 absorption in an adiabatic high-temperature metal hydride reactor based on thermochemical heat storage: MgH2 and Mg(OH)2 as reference materials, Int. J. Hydrogen Energy 42 (26) (2017) 16632–16644, https://doi.org/10.1016/j.ijhydene.2017.05.123.
[34] J. Vogel, M. Keller, M. Johnson, Numerical modeling of large-scale finned tube latent thermal energy storage systems, Journal of Energy Storage 29 (2020), 101389, https://doi.org/10.1016/j.est.2020.101389.
[35] Y. Ye, J. Ding, W. Wang, J. Yan, The storage performance of metal hydride hydrogen storage tanks with reaction heat recovery by phase change materials, Appl. Energy 299 (2021), 117255, https://doi.org/10.1016/j.apenergy.2021.117255.
[36] A. Chaise, P. de Rango, P. Marty, D. Fruchart, Experimental and numerical study of a magnesium hydride tank, Int. J. Hydrogen Energy 35 (12) (2010) 6311–6322, https://doi.org/10.1016/j.ijhydene.2010.03.057.
[37] N. Mallya, S. Haussener, Buoyancy-driven melting and solidification heat transfer analysis in encapsulated phase change materials, Int. J. Heat Mass Transf. 164 (2021), 120525, https://doi.org/10.1016/j.ijheatmasstransfer.2020.120525.
[38] J. Vogel, A. Thess, Validation of a numerical model with a benchmark experiment for melting governed by natural convection in latent thermal energy storage, Appl. Therm. Eng. 148 (2019) 147–159, https://doi.org/10.1016/j.applthermaleng.2018.11.032.
[39] S.S. Ardahaie, M. Hosseini, M. Eisapour, A. Eisapour, A. Ranjbar, A novel porous metal hydride tank for hydrogen energy storage and consumption assisted by PCM jackets and spiral tubes, J. Clean. Prod. 311 (2021), 127674, https://doi.org/10.1016/j.jclepro.2021.127674.
[40] A. Chibani, S. Merouani, N. Gherraf, Y. Benguerba, Thermodynamics and kinetics analysis of hydrogen absorption in large-scale metal hydride reactor coupled to phase change material-metal foam-based latent heat storage system, Int. J. Hydrogen Energy 47 (64) (2022) 27617–27632, https://doi.org/10.1016/j.ijhydene.2022.06.079.
[41] H. El Mghari, J. Huot, L. Tong, J. Xiao, Selection of phase change materials, metal foams and geometries for improving metal hydride performance, Int. J. Hydrogen Energy 45 (29) (2020) 14922–14939, https://doi.org/10.1016/j.ijhydene.2020.03.226.
[42] F. Bouzgarrou, S. Mellouli, T. Alqahtani, S. Algarni, Parametric study of a metal hydride reactor with phase change materials and heat pipes, Int. J. Energy Res. 46 (4) (2022) 4588–4598, https://doi.org/10.1002/er.7451.
[43] S. Garrier, B. Delhomme, P. de Rango, P. Marty, D. Fruchart, S. Miraglia, A new MgH2 tank concept using a phase-change material to store the heat of reaction, Int. J. Hydrogen Energy 38 (23) (2013) 9766–9771, https://doi.org/10.1016/j.ijhydene.2013.05.026.
[44] T. Alqahtani, S. Mellouli, A. Bamasag, F. Askri, P.E. Phelan, Thermal performance analysis of a metal hydride reactor encircled by a phase change material sandwich bed, Int. J. Hydrogen Energy 45 (43) (2020) 23076–23092, https://doi.org/10.1016/j.ijhydene.2020.06.126.
[45] S. Mellouli, E. Abhilash, F. Askri, S. Ben Nasrallah, Integration of thermal energy storage unit in a metal hydride hydrogen storage tank, Appl. Therm. Eng. 102 (2016) 1185–1196, https://doi.org/10.1016/j.applthermaleng.2016.03.116.
[46] L. Bartolucci, V.K. Krastev, On the thermal integration of metal hydrides with phase change materials: numerical simulation developments towards advanced designs, in: Tech. Rep., SAE Technical Paper, 2022, https://doi.org/10.4271/2022-24-0018.
[47] S.D. Lewis, P. Chippar, Analysis of heat and mass transfer during charging and discharging in a metal hydride - phase change material reactor, Journal of Energy Storage 33 (2021), 102108, https://doi.org/10.1016/j.est.2020.102108.
[48] Y. Ye, J. Lu, J. Ding, W. Wang, J. Yan, Performance improvement of metal hydride hydrogen storage tanks by using phase change materials, Appl. Energy 320 (2022), 119290, https://doi.org/10.1016/j.apenergy.2022.119290.
[49] K.V. Krishna, V. Pandey, M. Maiya, Bio-inspired leaf-vein type fins for performance enhancement of metal hydride reactors, Int. J. Hydrogen Energy 47 (56) (2022) 23694–23709, https://doi.org/10.1016/j.ijhydene.2022.05.163.
[50] A. Shahsavar, A. Goodarzi, I. Baniasad Askari, M. Jamei, M. Karbasi, M. Afrand, The entropy generation analysis of the influence of using fins with tip clearance on the thermal management of the batteries with phase change material: application a new gradient-based ensemble machine learning approach, Eng. Anal. Bound. Elem. 140 (2022) 432–446, https://doi.org/10.1016/j.enganabound.2022.04.024.
[51] W. Kong, G. Wang, G. Englmair, E.N.N. Nielsen, J. Dragsted, S. Furbo, J. Fan, A simplified numerical model of pcm water energy storage, Journal of Energy Storage 55 (2022), 105425, https://doi.org/10.1016/j.est.2022.105425.